The Astrophysical Journal, 679:797–812, 2008 May 20
© 2008. The American Astronomical Society. All rights reserved. Printed in U.S.A.

PLANET SHADOWS IN PROTOPLANETARY DISKS. I. TEMPERATURE PERTURBATIONS

Hannah Jang-Condell[1]
Department of Terrestrial Magnetism, Carnegie Institution of Washington, Washington, DC 20015; hannah@astro.umd.edu
Received 2007 October 19; accepted 2008 January 25

ABSTRACT

Planets embedded in optically thick passive accretion disks are expected to produce perturbations in the density and temperature structure of the disk. We calculate the magnitudes of these perturbations for a range of planet masses and distances. The model predicts the formation of a shadow at the position of the planet paired with a brightening just beyond the shadow. We improve on previous work on the subject by self-consistently calculating the temperature and density structures under the assumption of hydrostatic equilibrium and taking the full three-dimensional shape of the disk into account rather than assuming a plane-parallel disk. While the excursion in temperatures is less than in previous models, the spatial size of the perturbation is larger. We demonstrate that a self-consistent calculation of the density and temperature structure of the disk has a large effect on the disk model. In addition, the temperature structure in the disk is highly sensitive to the angle of incidence of stellar irradiation at the surface, so accurately calculating the shape of the disk surface is crucial for modeling the thermal structure of the disk.

Subject headings: planetary systems: formation — planetary systems: protoplanetary disks — radiative transfer

Online material: color figures

1. INTRODUCTION

Giant planets forming by core accretion need to have cores of $10-20\ M_\oplus$ to be massive enough to accrete a gaseous envelope (Hubickyj et al. 2005). This predicts that sizeable planet embryos form before circumstellar gas disks dissipate. These disks are typically modeled as passive accretion disks, optically thick and gas dominated. Their temperature structure is strongly dependent on heating from stellar irradiation (Chiang & Goldreich 1997; Calvet et al. 1991; D'Alessio et al. 1998, 1999a, 2001). In particular, the disk temperatures depend strongly on the angle of incidence of the stellar irradiation on the disk surface.

While a substantial amount of work on numerical hydrodynamic simulations of planets embedded in disks has been carried out, calculating the radiative transfer of stellar irradiation in conjunction with these simulations is prohibitively difficult. Simulations by Bate et al. (2003) illustrate the effect of hydrodynamics on the disk structure around a small embedded planet but use an isothermal equation of state. The effects of MHD turbulence have been studied by Papaloizou et al. (2004) and Oishi et al. (2007) but again, assuming a simple and unrealistic equation of state. Klahr & Kley (2006) and Paardekooper & Mellema (2006, 2008) have made an effort to include radiative transfer, as well as hydrodynamics, in their calculations, but do not include the effects of stellar irradiaton on their models.

The work presented in this paper does not include hydrodynamics, but rather focuses on the effects of stellar irradiation, which is a particularly important source of heating in the photospheres of disks. Since it is the photospheres of optically thick disks that are observed, the effects of stellar irradiation at the surface of disks are an important consideration in predicting observations of protoplanetary disks. A limitation of the hydrodynamic simulations described above is that in order to adequately model the densest regions of the gas they are necessarily limited in spatial range above the midplane. The photosphere and surface of a disk are often several scale heights above the midplane. The models presented here are complementary to detailed hydrodynamic simulations for this reason.

We are particularly interested in determining if the growing cores of giant planets produce effects that are observable. If these effects are observed, they would affirm the core accretion model as the paradigm for giant planet formation. While a fully formed Jupiter-mass planet would produce a larger feature in a disk, it would reveal little about how it formed.

Previous work on small planets embedded in optically thick gas disks indicates that sub-Jovian mass planet cores can perturb the disk enough to alter the temperature structure of the disk in the immediate vicinity of the planet, with consequences for further evolution of the planet (Jang-Condell & Sasselov 2003, 2004, 2005). In Jang-Condell & Sasselov (2003, 2004, hereafter Papers I and II, respectively), the planet is predicted to gravitationally compress the disk in the vertical direction, creating a shadow paired with a bright spot, leading to temperature variations. However, those models were limited by being plane parallel, despite the sizes of the simulation boxes used. In addition, while the density perturbations were calculated under hydrostatic equilibrium, they were not calculated self-consistently with the temperature perturbations.

In this paper, we improve on the model presented in Papers I and II by iteratively calculating the density and temperature structure of the disk for self-consistency and eliminating the assumption of a locally plane-parallel model. The paper is organized as follows: in § 2 we describe the basic model and the improvements that we have made, in § 3 we elaborate in detail on the method that we use for modeling radiative transfer, in § 4 we describe our results for different planet masses and distances, in § 5 we discuss our results in comparison to previous models, and in § 6 we present our conclusions.

2. MODEL CALCULATION

We adopt the formalism developed in Jang-Condell & Sasselov (2003, 2004) for calculating the effects on temperature of shadowing and brightening of stellar illumination at the disk's surface. These methods are based on those of Calvet et al. (1991) and D'Alessio et al. (1998, 1999a) in a one-dimensional (1D) plane-parallel disk.

[1] Current address: Department of Astronomy, University of Maryland, College Park, MD 20740-2421.

The improvements made on the previous model include iteratively calculating the temperature and density structure of the disk for self-consistency. The new model is not plane parallel as the previous models were. It accounts for the variation of disk structure with radius and the curvature of the disk in azimuth.

Each iteration proceeds as follows. Starting with the density structure of the disk, we calculate the temperature of the disk in radiative equilibrium with viscous heating and stellar irradiation as heating sources. We adapt methods developed in Papers I and II to calculate radiative transfer on the surface of a perturbed disk. Then, given the new temperature structure, we recalculate the density structure assuming vertical hydrostatic equlibrium.

Each of these steps is described in detail below. The initial conditions, which assume azimuthal symmetry, are calculated iteratively until they reach stability. The computationally intensive nature of the calculations prohibits large numbers of iterations when a planet is added, so relatively few iterations are carried out for the planet in the disk.

2.1. *Model Parameters*

We use rotating cyclindrical coordinates (r, ϕ, z) throughout, with the star at the origin, the planet at $(a, 0, 0)$, and the z-axis aligned with the orbital angular momentum vector. We adopt parameters for the stellar mass, radius, and effective temperature of $M_* = 1\ M_\odot$, $R_* = 2.6\ R_\odot$, and $T_* = 4280$ K, corresponding to an age of 1 Myr (Siess et al. 2000). The mass accretion rate is $\dot{M} = 10^{-8}\ M_\odot\ \mathrm{yr}^{-1}$, and the viscosity parameter is $\alpha_v = 0.01$, which are typical of T Tauri type stars.

The simulation box is centered on the planet at $(a, 0, 0)$. The size of the box is scaled relative to the Hill radius, $r_{\mathrm{Hill}} = a(m_p/3M_*)^{1/3}$. The box spans from $r_{\min} = a - 12.5r_{\mathrm{Hill}}$ to $r_{\max} = a + 12.5r_{\mathrm{Hill}}$ in r and from $\phi_{\min} = -12.5r_{\mathrm{Hill}}/a$ to $\phi_{\max} = 12.5r_{\mathrm{Hill}}/a$ in ϕ. The height of the box is set to $z_{\max} \sim 2z_s$, where z_s is the height of the unperturbed disk surface at $r = a$. We assume symmtery across the midplane, so $z_{\min} = 0$. The box is decomposed onto a grid of $100 \times 100 \times 100$ points equally spaced in r, ϕ, and z, with the grid slice at $\phi = \phi_{\min}$ used as a placeholder for structure of the unperturbed disk.

We use the opacities from D'Alessio et al. (2001), using a dust model with parameters $a_{\max} = 1$ mm, $T = 300$ K, and $p = 3.5$, assuming that the dust opacities are constant throughout the disk. The values for the opacities (in $\mathrm{cm}^2\ \mathrm{g}^{-1}$) are as follows: the Rosseland mean opacity is $\chi_{\mathrm{R}} = 1.91$, the Planck mean opacity integrated over the disk spectrum (300 K) is $\kappa_{\mathrm{P}} = 0.992$, and the Planck mean opacities integrated over the stellar spectrum (4000 K) are $\kappa^*_{\mathrm{P}} = 1.31$ for absorption alone and $\chi^*_{\mathrm{P}} = 5.86$ for absorption plus scattering. The absorption fraction is then $\alpha_{\mathrm{abs}} = \kappa^*_{\mathrm{P}}/\chi^*_{\mathrm{P}}$, while the scattered fraction is $\sigma = 1 - \alpha_{\mathrm{abs}}$. The Rosseland mean opacity is used to calculate the photosphere of the disk, and χ^*_{P} is used to calculate the surface of the disk.

2.2. *Heating Sources*

The basic calculation for radiative heating is described in detail in Jang-Condell & Sasselov (2003). Here we summarize those methods. The two main heating sources are from viscous heating (Γ_v) and stellar irradiation (Γ_r), offset by radiative cooling,

$$\Lambda = \rho\chi_{\mathrm{R}}\sigma_{\mathrm{B}}T^4, \tag{1}$$

where ρ is density, σ_{B} is the Stefan-Boltzmann constant, and T is the local temperature of the gas. Under equilibrium conditions,

$$\Gamma_v + \Gamma_r = \Lambda. \tag{2}$$

If T_v and T_r give the equilibrium temperature for solely viscous heating or stellar irradiation, respectively, then it follows that the equilibrium temperature given both sources of heating is

$$T_{\mathrm{eq}} = (T_v^4 + T_r^4)^{1/4}. \tag{3}$$

2.2.1. *Viscous Heating*

We assume that viscous flux is generated at the midplane and transported radiatively in a gray atmosphere so that

$$T_v = \left[\frac{3F_{v,\mathrm{ph}}}{8\sigma_{\mathrm{B}}}\left(\tau_d + \frac{2}{3}\right)\right]^{1/4}, \tag{4}$$

where τ_d is the optical depth perpendicular to the disk using the Rosseland mean opacity, χ_{R}: $\tau_d = \int_z^\infty \chi_{\mathrm{R}}\rho\ dz'$. The viscous flux emitted at the photosphere $F_{v,\mathrm{ph}}$ at a distance r for a star of mass $M_\star$ and radius $R_\star$ accreting at a rate $\dot{M}_a$ is (Pringle 1981)

$$F_{v,\mathrm{ph}} = \frac{3GM_\star\dot{M}_a}{4\pi r^3}\left[1 - \left(\frac{R_\star}{r}\right)^{1/2}\right]. \tag{5}$$

Viscous heating above the surface is assumed to be negligible.

2.2.2. *Stellar Irradiation*

The amount of heating from stellar irradiation is calculated using methods developed in Papers I and II for a plane-parallel disk and adapted for a fully three-dimensional (3D) system. The full details of this calculation are rather lengthy, so this has been set out in § 3.

2.2.3. *Differential Rotation*

The gas moves in streamlines past the planet at approximately the Keplerian rate, resulting in the shearing out of the hot and cold spots as material moves into and out of shadows and brightenings. The calculation is done in steady state, meaning that the gas is treated as a steady flow so that temperatures as a function of spatial position are constant even though the gas itself is in motion. Given the bulk velocity along a particular streamline, the movement of the gas from one grid cell to the next is equivalent to a time step equal to the length of the grid cell divided by the velocity.

The equilibrium temperature calculated in equation (2) represents the total amount of heating due to disk viscosity and stellar irradiation. We assume that the specific heat per unit surface area of the disk is $k\Sigma/\bar{m}$, where k is the Boltzmann constant and $\bar{m}$ is the mean molecular weight of the gas, which we assume to be primarily molecular hydrogen. Then we can approximate the rate at which a parcel of gas radiatively heats or cools as

$$\frac{k\Sigma}{m}\frac{\partial T}{\partial t} = \sigma_{\mathrm{B}}(T_{\mathrm{eq}}^4 - T^4). \tag{6}$$

If $T_{\mathrm{eq}} < T$, the parcel of gas cools; if $T_{\mathrm{eq}} > T$, the parcel of gas heats.

2.3. *Density Profile*

To calculate the density profile for the disk, we assume hydrostatic equilibrium,

$$\frac{1}{\rho}\frac{dP}{dz} = -g_z, \tag{7}$$

where ρ is the density, P is the pressure, and g_z is the z-component of gravity. We assume the ideal gas law, $P = \rho kT/\bar{m}$. In the absence of the planet, the sole contribution to the gravity is the star:

$$g_z = \frac{GM_* z}{(r^2 + z^2)^{3/2}}. \quad (8)$$

We use this equation to calculate the initial conditions. When a planet is added, the gravity has an additional contribution from the planet, so equation (8) becomes

$$g_z = \frac{GM_* z}{(r^2 + z^2)^{3/2}} + \frac{GM_p z}{(r^2 + r_p^2 - 2rr_p \cos\phi + z^2)^{3/2}}. \quad (9)$$

Given a vertical temperature profile, we calculate the density profile by integrating equation (7) from the top of the simulation box down the midplane. For the perturbed disk, we require conservation of the total surface density. In a standard viscous accretion disk, the surface density of the disk and temperature of the disk are coupled. Thus, for the initial disk we normalize the total integrated surface density

$$\Sigma = 2\int_0^\infty \rho\, dz', \quad (10)$$

with the surface density given by a steadily accreting viscous disk

$$\Sigma = \frac{\dot{M}}{3\pi\nu_v}\left[1 - \left(\frac{R_\star}{r}\right)^{1/2}\right], \quad (11)$$

where ν_v is the viscosity of the disk (Pringle 1981). We adopt a standard Shakura-Sunyaev viscosity (Shakura & Sunyaev 1973) with $\nu_v = \alpha_v c_0 H$, where α_v is a dimensionless parameter, c_0 is the sound speed at the midplane, and H is the thermal scale height, given by $H = c_0/\Omega_K$, where Ω_K is the Keplerian angular velocity.

3. 3D RADIATIVE TRANSFER OF STELLAR IRRADIATION

In this section, we describe the details of radiative transfer of stellar irradiation on the surface of a disk perturbed by a planet. These methods are based on the work of Calvet et al. (1991) and D'Alessio et al. (1998), which calculated the vertical temperature structure of a locally plane-parallel disk model without perturbations. In Papers I and II, we developed a method for using their solutions to calculate radiative transfer on a perturbed locally plane-parallel disk. Here we extend the formalism to a fully three-dimensional disk.

For a plane-parallel medium, the optical depth at disk-temperature frequencies perpendicular to the surface (τ_d) is related to the line-of-sight optical depth to stellar radiation (τ_s) as $\tau_s = \chi_P^* \tau_d/(\chi_R \mu)$, where μ is the angle of incidence of the stellar radiation at the surface. As shown in Paper II, T_r for a locally plane-parallel disk is given by

$$B(\tau_s) = \frac{\sigma_B T_r^4}{\pi} = \frac{\alpha_{abs} F_{irr}\mu}{4\pi}\left(c_1 + c_2 e^{-\tau_s} + c_3 e^{-\beta\mu\tau_s}\right), \quad (12)$$

where μ is the cosine of the angle of incidence of stellar irradiation at the surface of the disk, $\beta \equiv (3\alpha_{abs})^{1/2}$, and the stellar flux incident at the surface is

$$F_{irr} = \frac{\sigma_B T_*^4 R_*^2}{(r_s^2 + z_s^2)}, \quad (13)$$

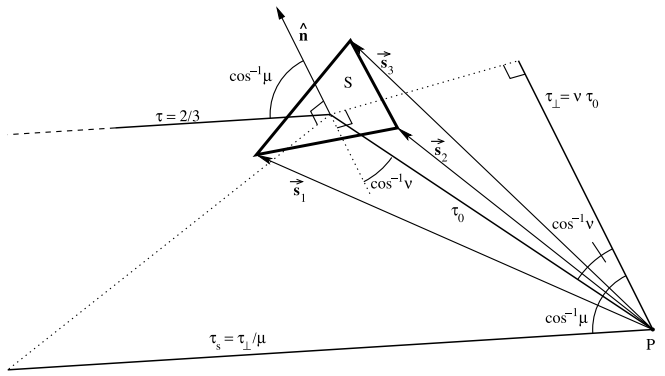

FIG. 1.—Angles used in calculating optical depths.

where (r_s, ϕ_s, z_s) are the coordinates at the surface. The remaining coefficients are

$$c_1 = \frac{6 + 9\mu\chi_R/\chi_P^*}{\beta^2} - \frac{6(1 - \chi_R/\chi_P^*)(3 - \beta^2)}{\beta^2(3 + 2\beta)(1 + \beta\mu)}, \quad (14)$$

$$c_2 = \left(\frac{\chi_P^*}{\mu\kappa_P} - \frac{3\mu\chi_R}{\chi_P^*}\right)\frac{(1 - 3\mu^2)}{(1 - \beta^2\mu^2)}, \quad (15)$$

$$c_3 = \left(\frac{\beta\chi_P^*}{\kappa_P} - \frac{3\chi_R}{\chi_P^*\beta}\right)\frac{(2 + 3\mu)(3 - \beta^2)}{\beta(3 + 2\beta)(1 - \beta^2\mu^2)}. \quad (16)$$

We adapt these equations to a three-dimensional disk by dividing the surface into grid elements by r_i and ϕ_j and numerically integrating the contributions from each surface element.

3.1. *Flux Contributions*

For a surface element δA located at S, the contribution to the flux at point $P = (r, \phi, z)$ in the disk is proportional to $B(\tau_s^{PS})$ as given in equation (12), with the optical depth calculated as

$$\tau_s^{PS} = \frac{2}{3} + \frac{\nu}{\mu}\int_P^S \chi_P^* \rho\, dl, \quad (17)$$

where the integral is carried out along the line segment $\overline{PS}$, and ν is the cosine of the angle between $\overline{PS}$ and the surface element. The geometry of the optical depth calculation is illustrated in Figure 1, where τ_s^{PS} is labeled as τ_s and $\tau_0 = \int_P^S \chi_P^* \rho\, dl$. The $\frac{2}{3}$ term on the left-hand side of equation (17) accounts for the optical depth from the star to the surface. The second term on the left-hand side of the equation is what τ_s would be between P and the infinite plane represented by the surface element. Defining $d\Omega$ to be the solid angle subtended by the surface element, then the total heating from stellar irradiation at P in the limit as $d\Omega \to 0$ is

$$B_{tot}(P) = \frac{1}{\pi}\int B(\tau_s^{PS}, \mu)\nu\, d\Omega. \quad (18)$$

For a plane-parallel disk this equation reverts to equation (12). To calculate this numerically over an assemblage of finite surface elements, we assume that $B(\tau_s^{PS}, \mu)$ stays fairly constant over a given surface element, and equation (18) becomes

$$B_{tot}(P) \approx \frac{1}{\pi}\sum_{\forall S} B(\tau_s^{PS}, \mu)\int_S \nu\, d\Omega. \quad (19)$$

The expression for $\int_S \nu\, d\Omega$ integrated over an arbitrary triangle with respect to P can be determined analytically as follows. We

define $\boldsymbol{s}_1$, $\boldsymbol{s}_2$, and $\boldsymbol{s}_3$ to be the vectors that point from P to the vertices of the triangle, as shown in Figure 1. Let $\hat{\boldsymbol{n}}$ be the unit normal to the triangle and θ_{ij} be the angle between the vectors $\boldsymbol{s}_i$ and $\boldsymbol{s}_j$. Then

$$\int_S \nu \, d\Omega = \hat{\boldsymbol{n}} \cdot \left[\frac{\theta_{12}}{\sin\theta_{12}} (\boldsymbol{s}_1 \times \boldsymbol{s}_2) + \frac{\theta_{23}}{\sin\theta_{23}} (\boldsymbol{s}_2 \times \boldsymbol{s}_3) + \frac{\theta_{31}}{\sin\theta_{31}} (\boldsymbol{s}_3 \times \boldsymbol{s}_1) \right]. \quad (20)$$

3.2. *Surface Decomposition*

We define the surface of the disk to be where the optical depth to stellar irradiation integrated along the line of sight is $\tau_s = \frac{2}{3}$. The optical depth at a given point $P = (r, \phi, z)$ in the disk is

$$\tau_s(r, \phi, z) = \tau_{\rm in} + \int_\ell \chi_{\rm P}^* \rho \, dl, \quad (21)$$

integrating along the line segment ℓ, which extends from the point toward the star, ending at the inner boundary of the box, at $(r_{\rm min}, \phi, z_{\rm in})$, where $z_{\rm in} = z r_{\rm min}/r$. The optical depth at the inner edge of the simulation box, $\tau_{\rm in}$, is assumed to be

$$\tau_{\rm in} = \frac{1}{2} \chi_{\rm P}^* \rho(r_{\rm min}, \phi, z_{\rm in}) \sqrt{r_{\rm min}^2 + z_{\rm in}^2}. \quad (22)$$

The density increases monotonically toward the midplane, so for every coordinate pair (r_i, ϕ_j) the height of the surface $h_{i,j}$ can be uniquely determined. The surface is defined by the set of points $\boldsymbol{s}_{i,j} = (r_i, \phi_j, h_{i,j})$.

The set of neighboring points, $\boldsymbol{s}_{i,j}, \boldsymbol{s}_{i+1,j}, \boldsymbol{s}_{i+1,j+1}$, and $\boldsymbol{s}_{i,j+1}$, define a surface element over which radiative transfer from stellar irradiation is calculated. The midpoint of this set of four points is

$$\boldsymbol{s}_m = \left[\left(\frac{r_i + r_{i+1}}{2} \right) \cos\left(\frac{\phi_{j+1} - \phi_j}{2} \right), \frac{\phi_j + \phi_{j+1}}{2}, \frac{h_{i,j} + h_{i+1,j} + h_{i+1,j+1} + h_{i,j+1}}{4} \right].$$

For the unperturbed disk, $h_{i,j}$ is independent of j, and $\boldsymbol{s}_{i,j}, \boldsymbol{s}_{i+1,j}$, $\boldsymbol{s}_{i+1,j+1}$, and $\boldsymbol{s}_{i,j+1}$ are coplanar. If $\hat{\boldsymbol{n}}$ is the normal to the plane through these four points, then the cosine of the angle of incidence is

$$\mu = \hat{\boldsymbol{s}}_m \cdot \hat{\boldsymbol{n}} + \frac{4R_*}{3\pi|\boldsymbol{s}_m|}, \quad (23)$$

where the second term on the right side of the equation is the minimum allowed value of μ, resulting from the finite size of the star. Note that in Papers I and II, we neglected to include this term in calculating μ, which resulted in more marked shadowing in the disk.

For the perturbed disk, the points $\boldsymbol{s}_{i,j}, \boldsymbol{s}_{i+1,j}, \boldsymbol{s}_{i+1,j+1}$, and $\boldsymbol{s}_{i,j+1}$ are not necessarily coplanar. In this case we subdivide the surface element into four triangles defined by the midpoint and two adjacent points, i.e., $(\boldsymbol{s}_{i,j}, \boldsymbol{s}_{i+1,j}, \boldsymbol{s}_m)$, $(\boldsymbol{s}_{i+1,j}, \boldsymbol{s}_{i+1,j+1}, \boldsymbol{s}_m)$, $(\boldsymbol{s}_{i+1,j+1}, \boldsymbol{s}_{i,j+1}, \boldsymbol{s}_m)$, and $(\boldsymbol{s}_{i,j+1} \boldsymbol{s}_{i,j}, \boldsymbol{s}_m)$, with normal vectors $\hat{\boldsymbol{n}}_1, \hat{\boldsymbol{n}}_2, \hat{\boldsymbol{n}}_3$, and $\hat{\boldsymbol{n}}_4$, respectively. The angles of incidence are calculated as $\mu_i = \hat{\boldsymbol{s}}_m \cdot \hat{\boldsymbol{n}}_i + 4R_*/(3\pi|\boldsymbol{s}_m|)$, and the contributions to radiative heating are summed over each triangle individually, with $F_{\rm irr}$ calculated at $\boldsymbol{s}_m$ for all of them.

In order to avoid a discontinuity of temperature above the surface of the disk, the temperature above the surface is taken to be $B(\tau_s, \mu)$, where μ is now the angle of incidence to the surface of constant τ_s:

$$\mu = \frac{\boldsymbol{r} \cdot \nabla \tau_s}{|\boldsymbol{r}||\nabla \tau_s|}. \quad (24)$$

Surface elements outside the simulation box are assumed to follow the same structure as the initial conditions, i.e., unperturbed by a planet. Regions with $|\phi| \geq \phi_{\rm max}$ are approximated as "strips" extending from $\phi_{\rm max}$ to $\pi/2$ and $-\phi_{\rm max}$ to $-\pi/2$. The surfaces interior to $r_{\rm min}$ and exterior to $r_{\rm max}$ are approximated as power laws ($h \propto r^a$) and integrated over as a series of infinite-length strips extending in the ϕ-direction.

3.3. *Initial Conditions*

Since we will be calculating the perturbed disk iteratively to take into account feedback between temperature and density perturbations, the initial disk itself must be stable to iterative feedback. We calculate the initial conditions for a slice in the middle of a box twice the size in ϕ-space. That is, the slice is at $\phi = 0$ in a box ranging from $-2\phi_{\rm max}$ to $2\phi_{\rm max}$, with twice the number of grid points in ϕ, and the same range of r and z. Outside the range of ϕ, the surface of the disk is approximated as strips from $2\phi_{\rm max}$ to $\pi/2$. Outside the range of r, the surface is approximated as strips with infinite length in the ϕ-direction, with the height z varying as a power law in r, fitted to the eight points at the ends of the box.

The unperturbed (i.e., without planet) structure of the disk is calculated iteratively as described above, but since azimuthal symmetry is assumed, this computation is significantly shorter than the computation of the perturbed disk structure. Thus, we iterate until the rms change in disk height is less than 10^{-6}, typically less than about 200 iterations.

We examine planets at $a = 1$, 2, 4, and 8 AU with masses of 10, 20, and 50 $M_\oplus$. The sizes and positions of the simulation boxes for each of these parameters are indicated in Figure 2. The limits of the simulation boxes in the r-direction are indicated by straight vertical lines: dotted, dashed, and solid for 10, 20, and 50 $M_\oplus$ planets, respectively. The boxes span from $r_{\rm min} = a - 12.5 r_{\rm Hill}$ to $r_{\rm max} = a + 12.5 r_{\rm Hill}$ in r and from 0 to $z_{\rm max} \sim 2z_s$, where z_s is the height of the unperturbed disk surface at $r = a$.

The left set of plots in Figure 2 show the density contours of the initial conditions for each set of planet parameters, dotted, dashed, and solid curves for 10, 20, and 50 $M_\oplus$ planets, respectively. The lower plot is a blow-up of the gray-outlined box in the upper plot. The density contours show a good amount of overlap over the range of parameter space.

The right set of plots in Figure 2 is similar to the left set, except that it shows temperature rather than density. The temperature contours do not overlap as well as the density contours, particularly at larger radii. At the planets' positions, the temperature contours converge fairly well, but tend to diverge at the boundaries of the simulations. This results from the sensitivity of the temperature structure to the density structure of the disk. At small distances, the temperatures are dominated by viscous heating, so the shape of the surface is less relevant. However, viscous heating drops off more rapidly than stellar irradiation heating, so at large distances, slight deviations in the calculation of the surface can lead to changes of several degrees in the vertical temperature structure of the disk. The discrepancies in temperature may be overcome by increasing the size of the simulation box. However, this leads to a corresponding increase in the computation time. Since the difference in temperatures tends to be on the order of just a few degrees and

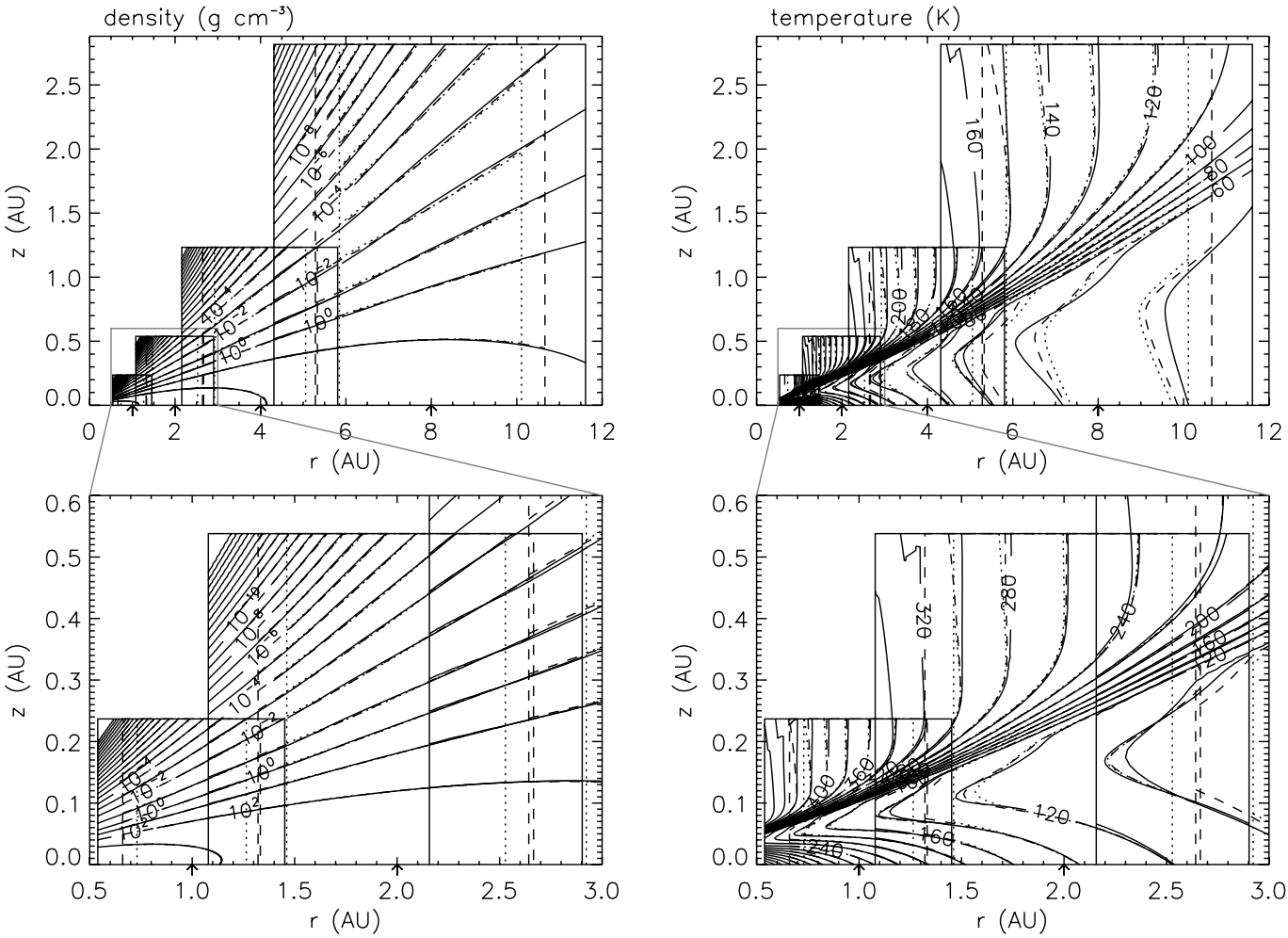

FIG. 2.— Initial density (*left*) and temperature (*right*) profiles for the planet masses and distances studied in this paper. The lower set of plots are blow-ups of the area delimited by gray lines. Positions of planets at 1 (*red*), 2 (*magenta*), 4 (*blue*), and 8 (*green*) AU are indicated by arrows along the *r*-axis. The density and temperature contours are indicated by dotted, dashed, and solid curves for 10, 20, and 50 $M_\oplus$ planets, respectively. [*See the electronic edition of the Journal for a color version of this figure*.]

since we are interested in the changes in disk structure due to the influence of a planet in the disk, at this time we will adopt the initial conditions as presented here.

4. RESULTS

The planet is instantaneously inserted into the initial conditions, and the resulting density and temperature perturbations are calculated. The density and temperature are then iteratively recalculated under the assumption of hydrostatic equilibrium for 10 iterations. Because the planet is instantaneously inserted into the disk and hydrostatic equilibrium is assumed, there is no timescale associated with each iteration. Rather, the goal is to iterate until steady state is achieved. When evolution is discussed in this paper in the context of our disk-planet models, we refer to the changes in disk structure over successive iterations rather than a time sequence.

4.1. *Self-Consistency: Effect of Iteration*

The iterative calculation was implemented to achieve self-consistency between the temperature and density profiles of the disk under hydrostatic equilibrium. This self-consistency proves to be important to determining the structure of the disk. As an example, we examine the case of a 20 $M_\oplus$ planet at 4 AU. In Figure 3 we show the evolution of the surface perturbation (*left*) and corresponding evolution of the temperature in the photosphere of the disk (*right*). The sequence of plots goes from left to right, top to bottom. The gray shaded circle shows the projected size of the Hill sphere, looking down on the disk along the *z*-axis.

Contours in the left panel show the fractional deviation of the surface at the given iteration number from the initial conditions, spaced at intervals of 0.002. Contours in the right panel show temperatures in the photosphere of the disk, where the photosphere is defined to be where the optical depth using the Rosseland mean opacity integrated along the *z*-axis from $z \rightarrow \infty$ toward $z = 0$ equals $\frac{2}{3}$. Although the perturbation is quite subtle, less than 2%, the change in the temperature at the photosphere is dramatic by comparison, on the order of 10% or more.

With successive iterations the perturbation to the surface grows in area and deepens. This is seen in both the surface contours and photospheric temperatures. This is because the region in shadow cools and compresses, deepening the shadow further still. Beyond the shadow, where the disk rises above the shadow, material heats and expands, causing this material to rise still further. The growth of the perturbation is limited both because of the differential rotation of disk material and because of the intrinsic radial temperature variation of the disk. The differential rotation of the disk means that material more radially distant from the planet moves past the planet faster, so it has less time to heat or cool as it passes by the

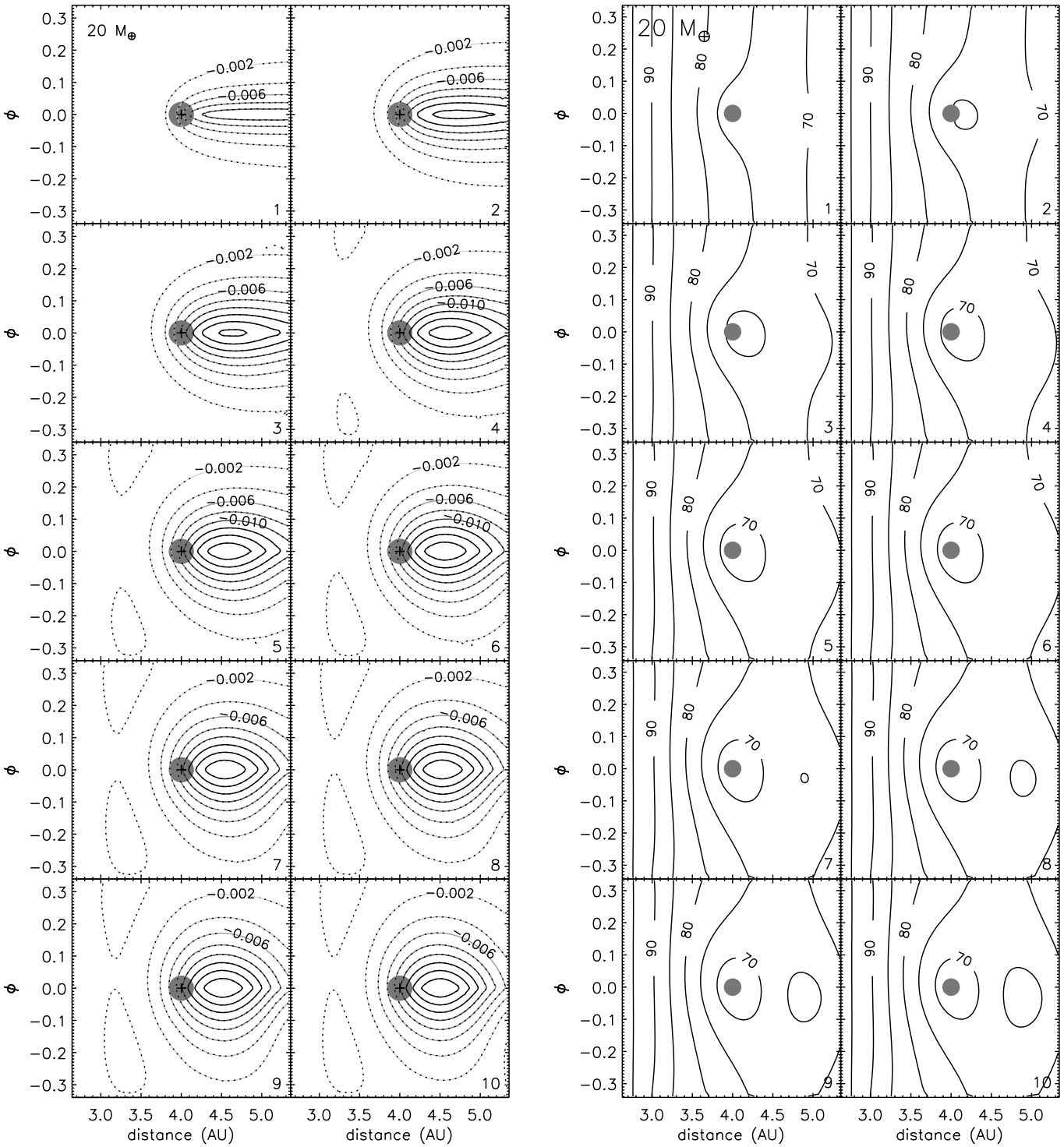

FIG. 3.— Evolution of the surface (*left*) and photosphere temperature (*right*) for a 20 $M_\oplus$ planet at 4 AU. The iteration number is indicated at the lower right in each individual plot. *Left*: Deviation of the surface from the initial conditions displayed as contours, in units of AU. The gray circle is a Hill radius in size, centered at the planet's location. *Right*: Contour plots of temperatures in the photosphere, in kelvins.

planet. The intrinsic temperature structure of the disk means that inward (outward) of the planet, the disk is hotter (cooler), limiting the growth of the shadow (brightened region) in that direction. Iterations 8–10 show very little difference between each other, indicating that the density and temperatures have reached self-consistency.

Figure 4 shows another view of the effect of iteration on the temperature structure of the disk. Here we plot the temperature cross section of the disk at $\phi = 0$, the location of the planet. The size of the Hill sphere is represented by the gray ellipse (the *r*- and *z*-axes are not scaled to each other). The surface layers are relatively unaffected by the changing density structure, largely because this region is optically thin, and the dependence of temperature on angle of incidence is small. The midplane layer is relatively unaffected as well. This is due to several effects: viscous heating is greatest at the midplane; the angular sizes of the shadowed/brightened regions are small; and the disk is optically thick. The intermediate layers change in temperature structure quite a bit. The development of a cooled region directly above the planet and the heated region outward from the planet are quite clearly evident.

Meanwhile, the density structure changes only subtly. In Figure 5, we plot the density contours for the $\phi = 0$ slice of the simulation box after 1 (*dotted lines*) and 10 (*solid lines*) iterations. Over the 10 iterations, the density contours do change, but not as dramatically as the temperature perturbations. This emphasizes the importance of the detailed density structure to the calculation of radiative transfer in the disk.

4.2. *Variations with Planet Mass and Distance*

We investigate the changes to the disk temperature structure as planet mass and distance vary. We examine planets with masses of 10, 20, and 50 $M_\oplus$ at 1, 2, 4, and 8 AU. Figure 6 summarizes the changes in photosphere temperatures for this suite of planet parameters. The contours in each of these plots indicate the absolute temperatures, while the gray scale reflects the fractional temperature variation from the initial conditions, dark for cooling and lighter for heating. In general, the cooled region is centered at the planet's position, while the heated region is outside the planet's orbit. The asymmetry in the perturbations is a result of including the differential rotation of the disk and a finite timescale for cooling/heating as a parcel of gas passes through a shadow/brightening. The sizes of the perturbations roughly scale with both planet mass and distance.

In Figures 7–10 we show radial cross sections of the temperature structure at (*from left to right*) 1 Hill radius downstream from the planet, at the planet position, and 1 Hill radius upstream of the planet, for the planet parameters examined in this study. The solid lines show the temperature contours, while the gray scale shows the amount of deviation from the initial conditions. Figures 7, 8, 9, and 10 show planets at 1, 2, 4, and 8 AU, respectively. For reference, the locations of the photospheres are indicated as black dotted lines. Also shown are the surface of the disk (*white dot-dashed line*) and thermal scale height (*black dashed line*). Both the photosphere and surface are multiple scale heights above the disk, except just above the Hill sphere. Temperature perturbations tend to be greatest in the upper layers of the disk, between the photosphere and the surface. Again, this is because of viscous heating at the midplane, as well as optical depth effects.

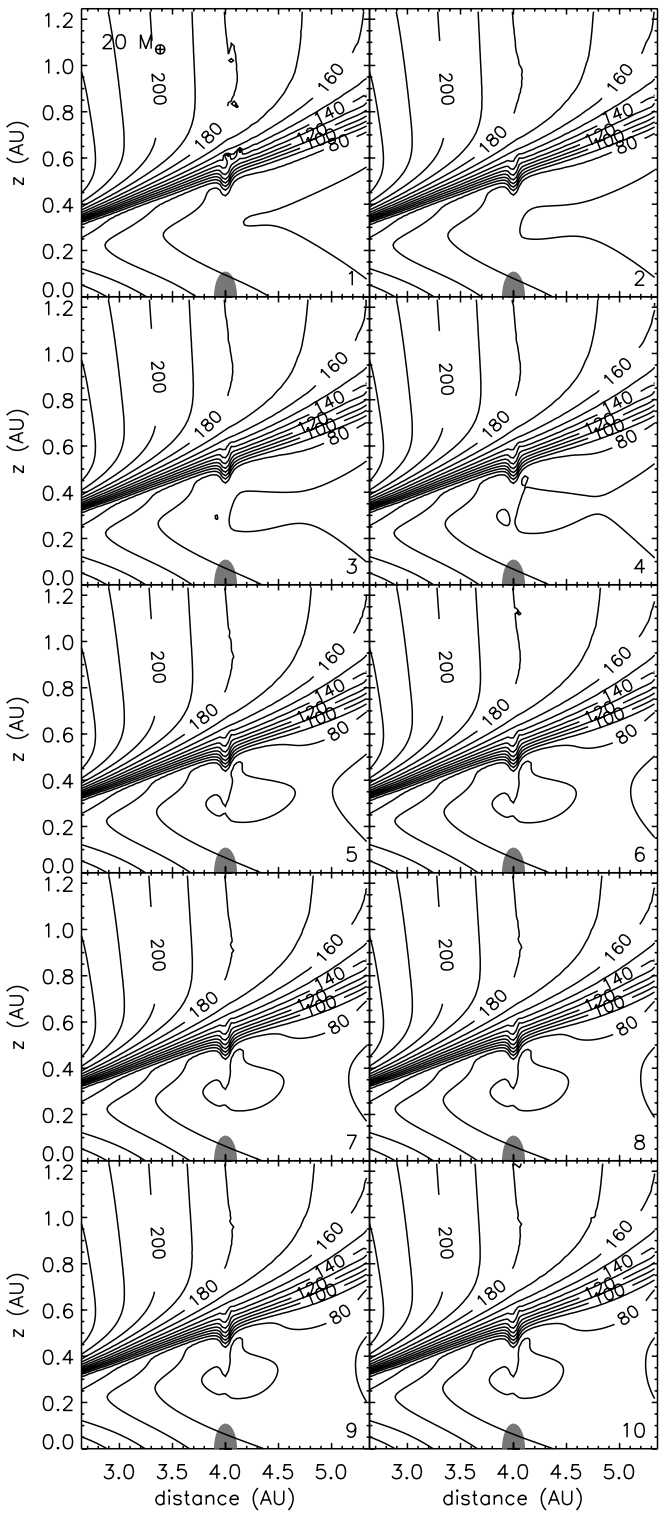

FIG. 4.—Evolution of temperatures in a cross section of the disk at $\phi = 0$ for a 20 $M_\oplus$ planet at 4 AU. The Hill radius and position of the planet are indicated by the gray half ellipse. The temperatures are indicated by contours, with the iteration number indicated at the lower right in each individual plot.

5. DISCUSSION

5.1. *Comparison to Previous Models*

We now compare our results to those of Papers I and II. The results presented there were for planets around a star of 0.5 $M_\odot$, while those presented here are for a 1 $M_\odot$ star. In order to make a fair comparison, we have recomputed the model presented in Papers I and II for the stellar parameters used in this paper. We will henceforth refer to this set of models as the J-CS model.

In Figure 11 we compare the results from this paper to J-CS for the case of a 20 $M_\oplus$ planet at 4 AU from its host star. The top plot shows the radial temperature cross section through the planet's

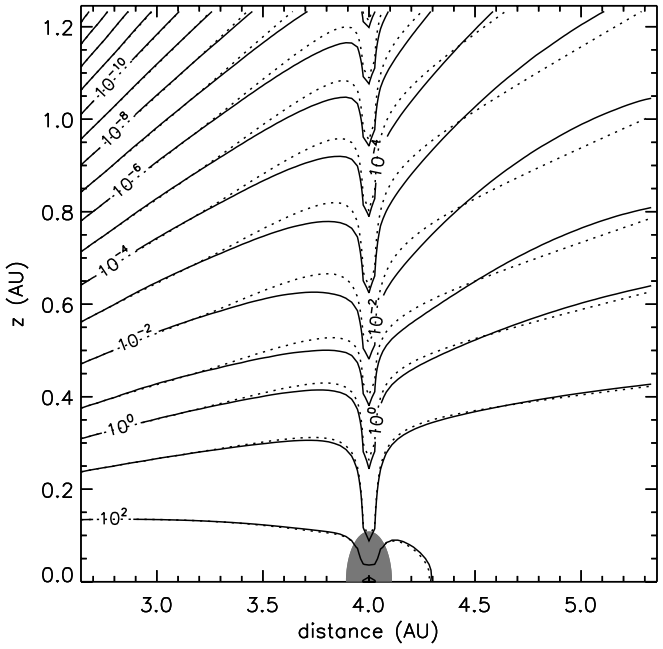

FIG. 5.— Evolution of densities in a cross section of the disk at $\phi = 0$ for a 20 $M_{\oplus}$ planet at 4 AU. The Hill radius and position of the planet are indicated by the gray half ellipse. The density varies subtly with successive iterations, so only density contours after the first iteration (*dotted lines*) and 10th iteration (*solid lines*) are shown.

position for J-CS, and the bottom shows the same cross section for the new model. In the J-CS model, the disk is treated as locally plane parallel, whereas in the new model it is not. This is reflected in the shape of the temperature structures of the two models. Another difference is that the surface was calculated as the contour of constant density in J-CS. This contour is shown as a red dot-dashed line. When this contour is shadowed, the surface is instead taken to be the line of sight to the star, indicated by the solid red line. In contrast, the new model calculates the surface to be where the optical depth to the star using the Planck mean extinction, $\chi_{\rm P}^{*}$, is $\frac{2}{3}$.

In J-CS, the temperature perturbations are more dramatic than in the new model. This can also be seen in Figure 12, which shows the temperatures in the photosphere compared side by side. The plots show temperature contours and fractional temperature variations, with the older model represented on the left. The right plot in this figure is the same as the one in Figure 6. The spatial sizes and color scalings are the same between the two plots. It is evident from both Figures 11 and 12 that the temperature perturbations are much greater in J-CS. The reason for this is primarily the way in which the surface was calculated. As noted in Paper I, the disk temperature structure is quite sensitive to μ, the cosine of the angle of incidence of stellar irradiation at the surface. In other words, the slope of the surface determines the amount of heating from stellar irradiation. Small deviations at the surface can lead to large temperature perturbations at the photosphere of the disk.

In the JC-S model, $\mu \rightarrow 0$ in the shadowed region, which means that zero flux was propagated from shadowed surface elements to disk material below them. When the density contour rose back above the shadow, the transition from shadow to the illuminated region was quite sharp, with relatively large values of μ yielding large amounts of heating. In the new model, since the surface is calculated by integrating the optical depth along lines of sight to the star, the transitions are smoother and values of μ do not vary as greatly. Also, as shown in equation (23), we set a minimum value for μ based on the finite size of the star, so shadowing cannot result in as significant cooling as seen in J-CS. Yet another effect is the radial variation in stellar flux, which was not taken into account in the plane-parallel J-CS model. The disk is hotter/cooler closer to/farther from the star, which offsets some of the effects of shadowing/illumination. Although the J-CS model was not iterative while the new model is, the changes in the calculation of the surface and μ are sufficient to diminish the temperature perturbations near the planet.

Another difference between J-CS and this work is the locations of the heated and cooled regions. In J-CS, these regions are nearly symmetric with respect to the planet position. The sizes and shapes of the heated and cooled regions are similar, with the cooled region inward of the planet and the heated region outward of it. In the current work the cooled region is centered on the planet's position, with the heated region outward of the planet.

5.2. *Magnitude of Temperature Variations*

In Paper II we found a correlation between the maximum and minimum photosphere temperature variations and the Hill radius of the planet. We now perform the same analysis on the new model.

In Figure 13, we plot the maximum and minimum fractional temperature variations in the photospheres versus the ratio of the Hill radius to thermal scale height of the disk ($r_{\rm Hill}/h$). Points above/below $\Delta T/T = 0$ represent maxima/minima. The symbols denote at what distance the planet is: triangles for 1 AU, diamonds for 2 AU, squares for 4 AU, and asterisks for 8 AU. The results for J-CS are plotted connected by dashed lines. As noted in Paper II, the maxima and minima lie nearly on the same curves. The upturn in minimum temperatures at smaller distances is due to the rise in viscous heating closer to the star, which sets the absolute temperature minimum.

The points connected by dotted lines in Figure 13 are temperature maxima/minima in the photospheres after one iteration, i.e., without recalculating the density given the new temperature structure. These points similarly lie on nearly the same curves, except showing a much smaller temperature perturbation than JC-S. The reasons for the smaller temperature variation were detailed in § 5.1.

The effect of including iterations can be seen by comparison to the points connected by solid lines in Figure 13. In all cases, the fractional temperature variations increase. However, the amount of change is not consistent with planet mass or distance. At 1 AU (*triangles*), the change in temperature minima is nearly negligible. This can be explained by viscous heating, which halts the growth of the cooled, shadowed region. The temperature maxima do increase, but not as much as at larger distances. This is because the growth of the brightened region is coupled to the growth of the shadowed region: as the shadowed region grows, more disk material behind the shadow is exposed and illuminated. Since shadow growth is limited at 1 AU, so is the growth of the brightened region. Going from 2 to 4 to 8 AU, viscous heating ceases to be important. The temperature maxima all lie close to the same curve at those distances, and the temperature minima at 4 and 8 AU lie nearly on the same curve in Figure 13.

For larger planets, those whose Hill radii approach the disk thermal scale height, the amount of heating in the current model approaches that seen in J-CS. However, the temperature minima never drop that low. This can be attributed to the minimum value of μ that has been adopted for the new model. There is such an upper limit that has been imposed, however, hence the greater heating.

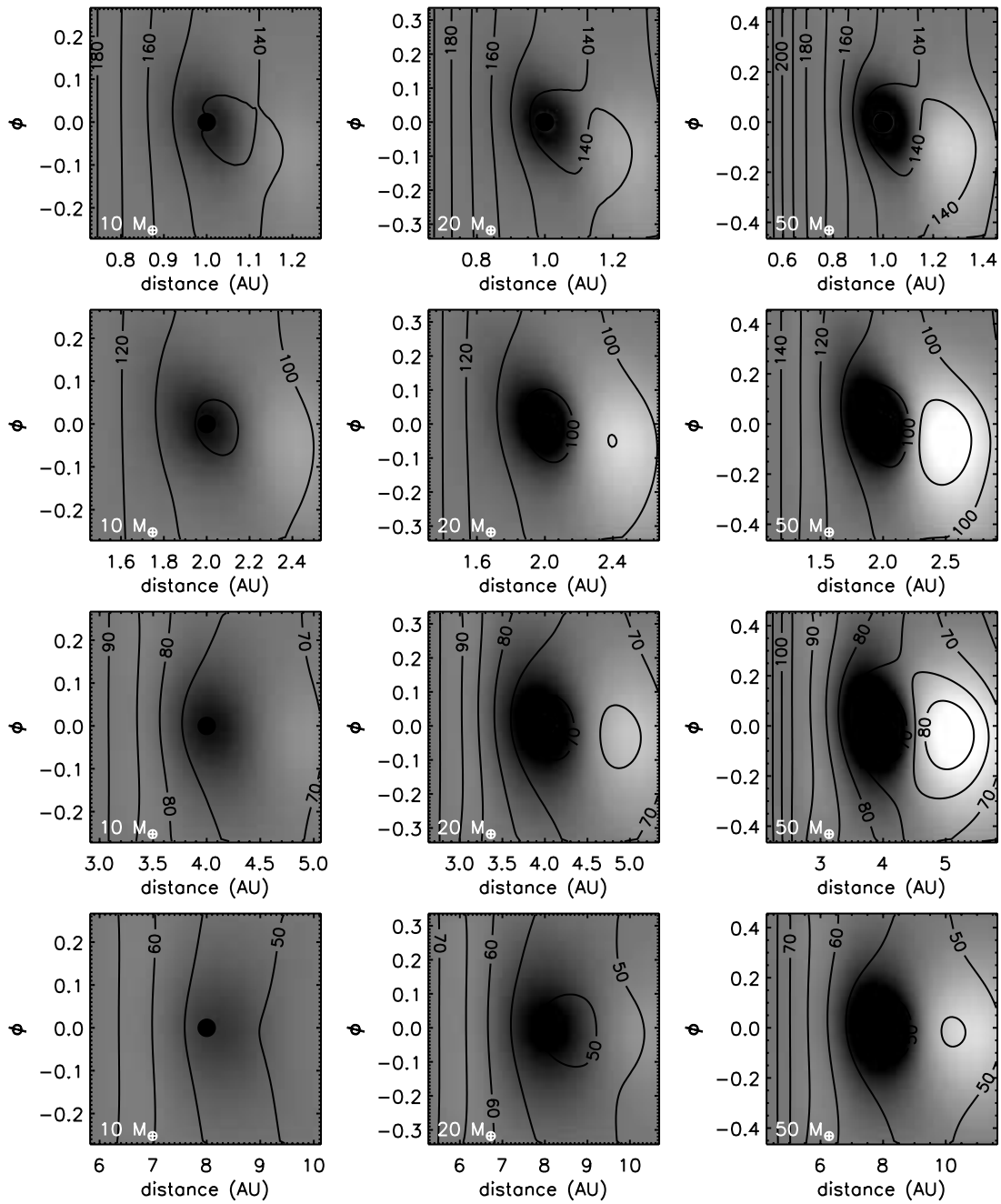

FIG. 6.—Temperatures in the photospheres of disk models with planets after 10 iterations. *From top to bottom:* planets at 1, 2, 4, and 8 AU. *From left to right*: planets with mass 10, 20, and 50 $M_{\oplus}$. The region above the Hill sphere is blacked out. Solid contours indicate temperatures in kelvins. The shading shows the fractional deviation in temperature from the initial disk model, so that black is $\Delta T/T = -0.2$ and white is $\Delta T/T = +0.2$.

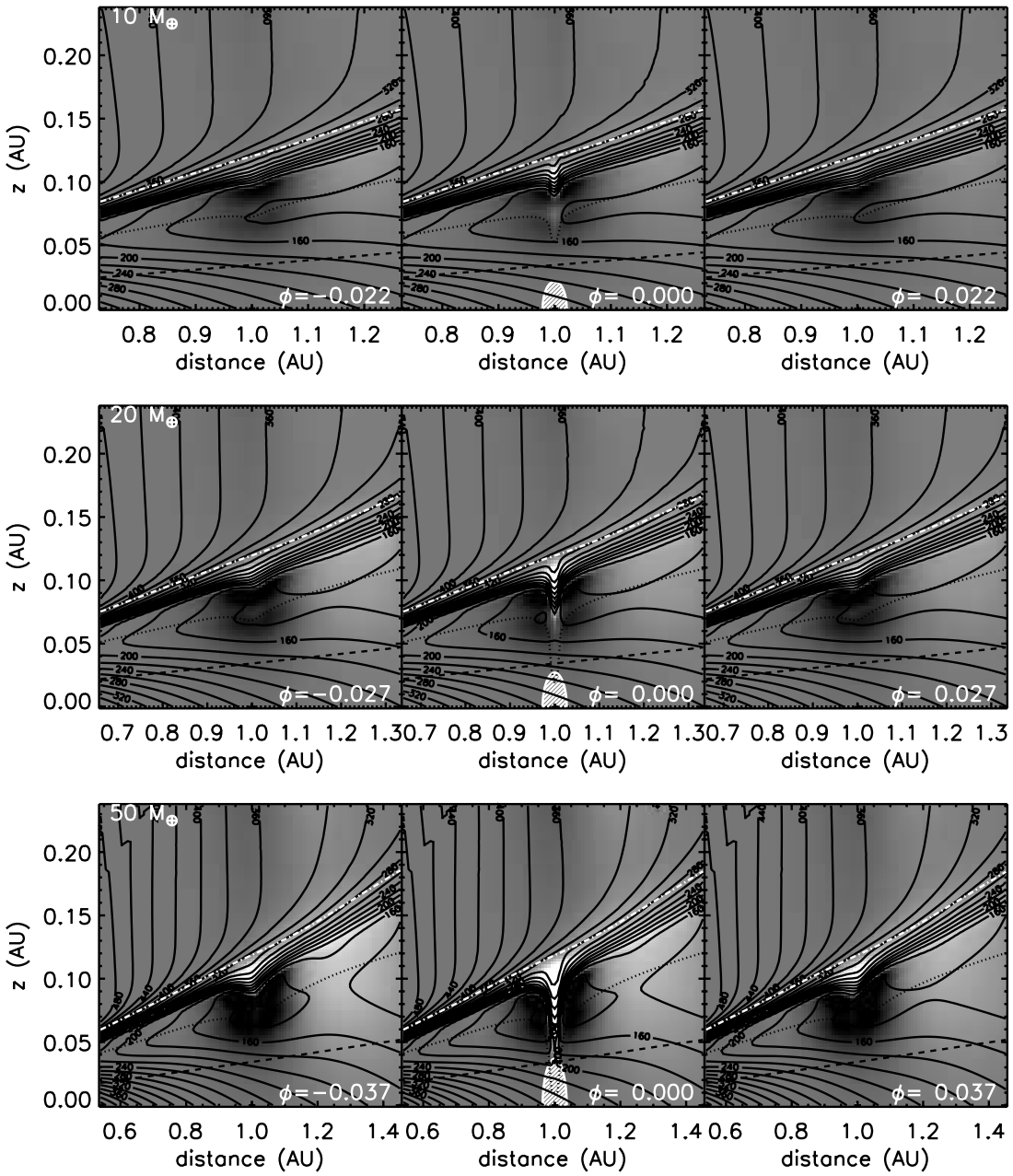

FIG. 7.— Temperature cross sections of the disk in the vicinity of a planet at 1 AU from a 1 $M_\odot$ star at the indicated azimuthal angles, corresponding to (*from left to right*) $1r_{\rm Hill}$ downstream of the planet, at the planet position, and $1r_{\rm Hill}$ upstream of the planet. The location and size of the Hill sphere are indicated by the white hashed area. From top to bottom, planet masses are 10, 20, and 50 $M_\oplus$. The contours show absolute temperatures while the color scale shows the fractional temperature difference from the initial disk model, with a range of $\Delta T/T \in [-0.2, +0.2]$.

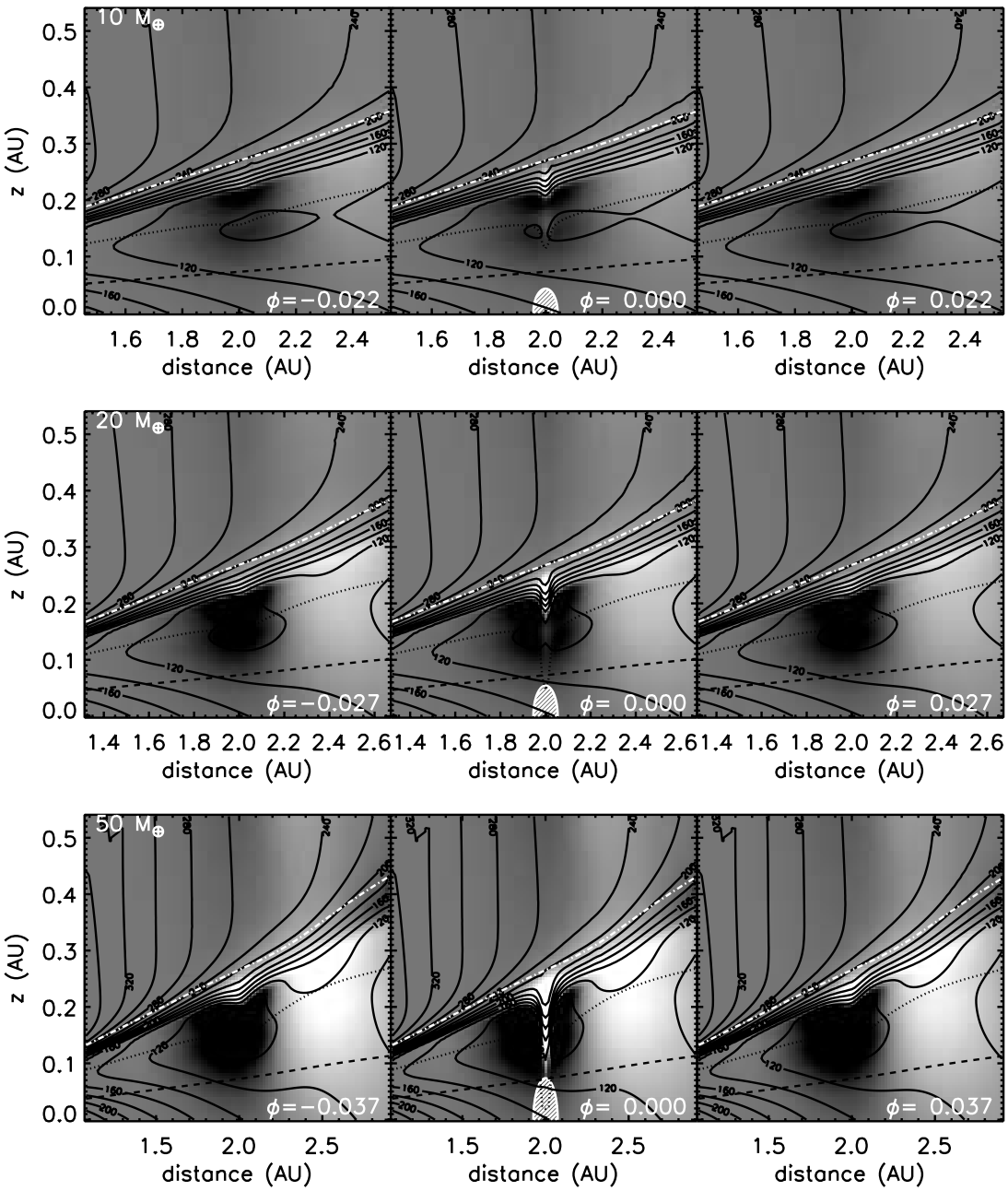

FIG. 8.— Same as Fig. 7, but for planets at 2 AU.

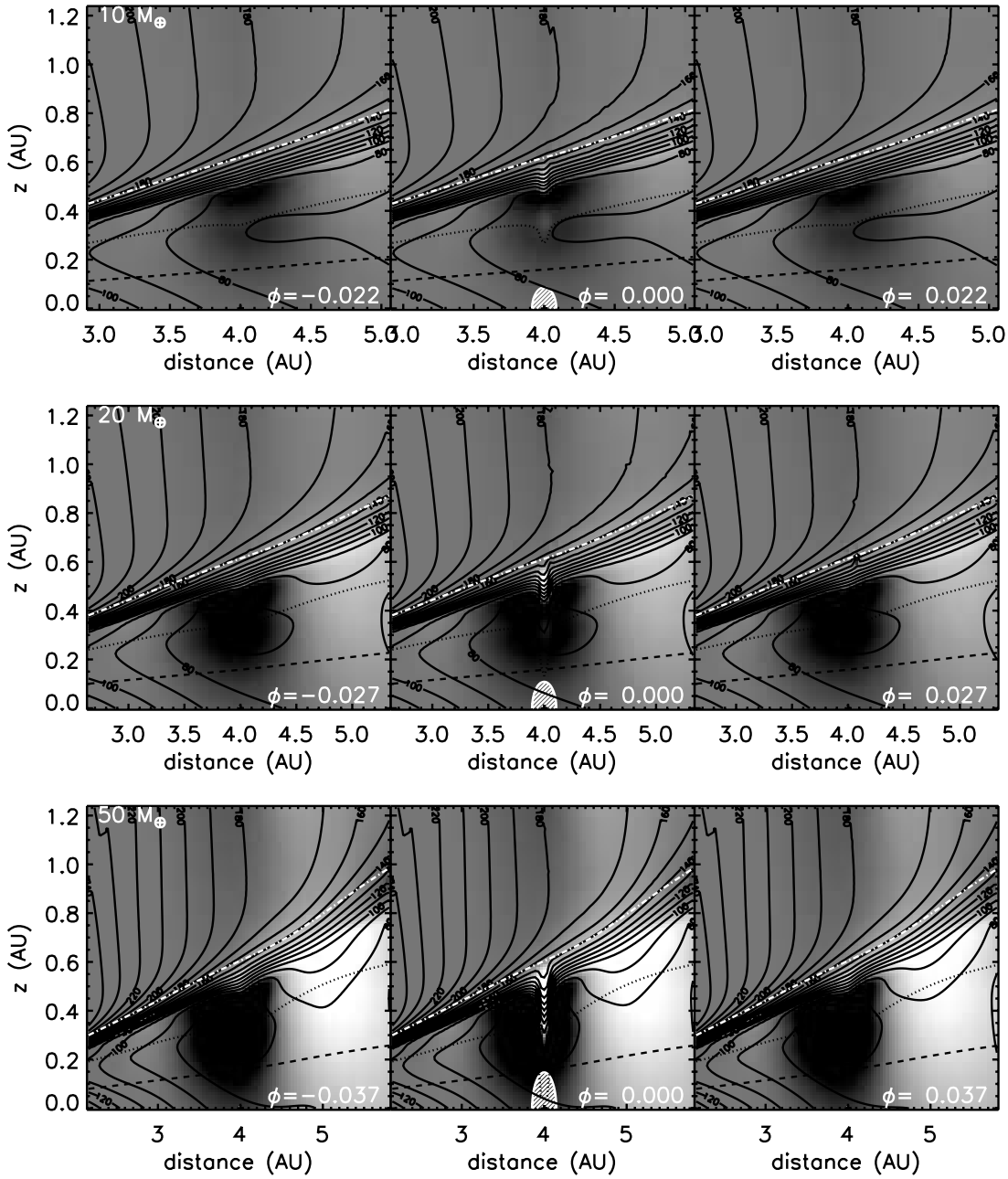

FIG. 9.—Same as Fig. 7, but for planets at 4 AU.

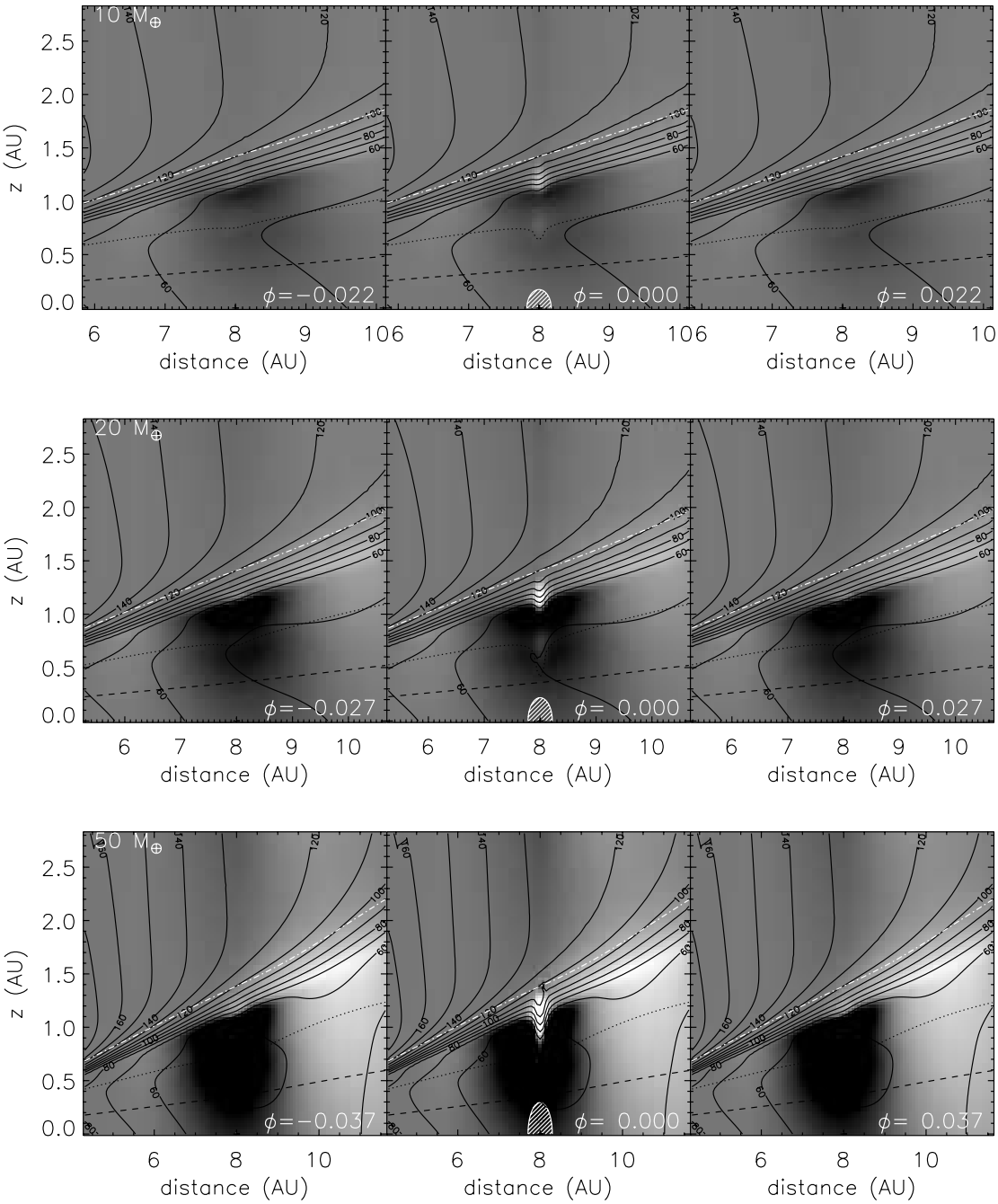

FIG. 10.— Same as Fig. 7, but for planets at 8 AU.

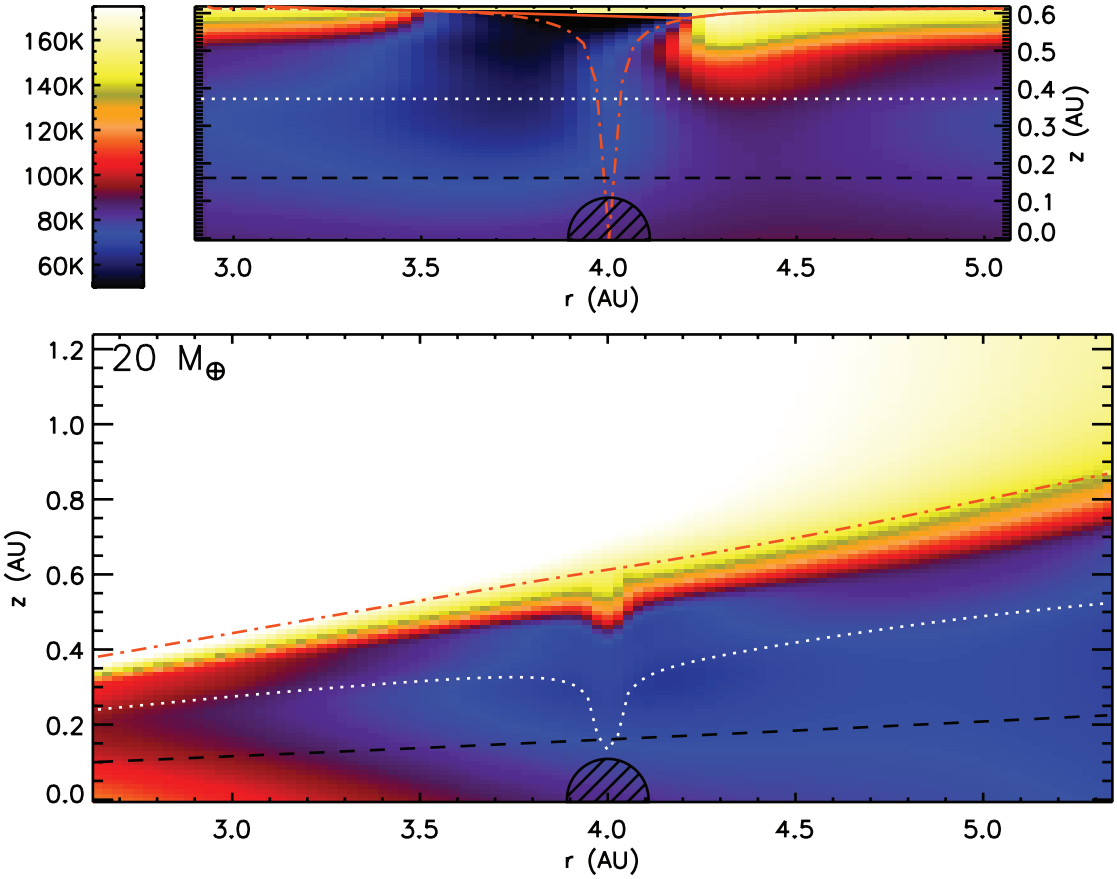

FIG. 11.— Thermal structure of the disk in the vicinity of a 20 $M_\oplus$ planet at 4 AU from a 1 $M_\odot$ star, as calculated for J-CS (*top*) and this paper (*bottom*). The temperatures are scaled to the same colors, and the *r*- and *z*-axis have the same scaling. The hashed semicircle shows the size and location of the Hill sphere. The photosphere is indicated by white dotted lines, and the thermal scale height is indicated by black dashed lines. In the top plot the red dot-dashed line shows the isodensity contour equal to the density at the disk surface. Regions below the solid red line in the top plot are considered to be in shadow. In the bottom plot the red dot-dashed line is the surface as calculated from line-of-sight optical depth to the star.

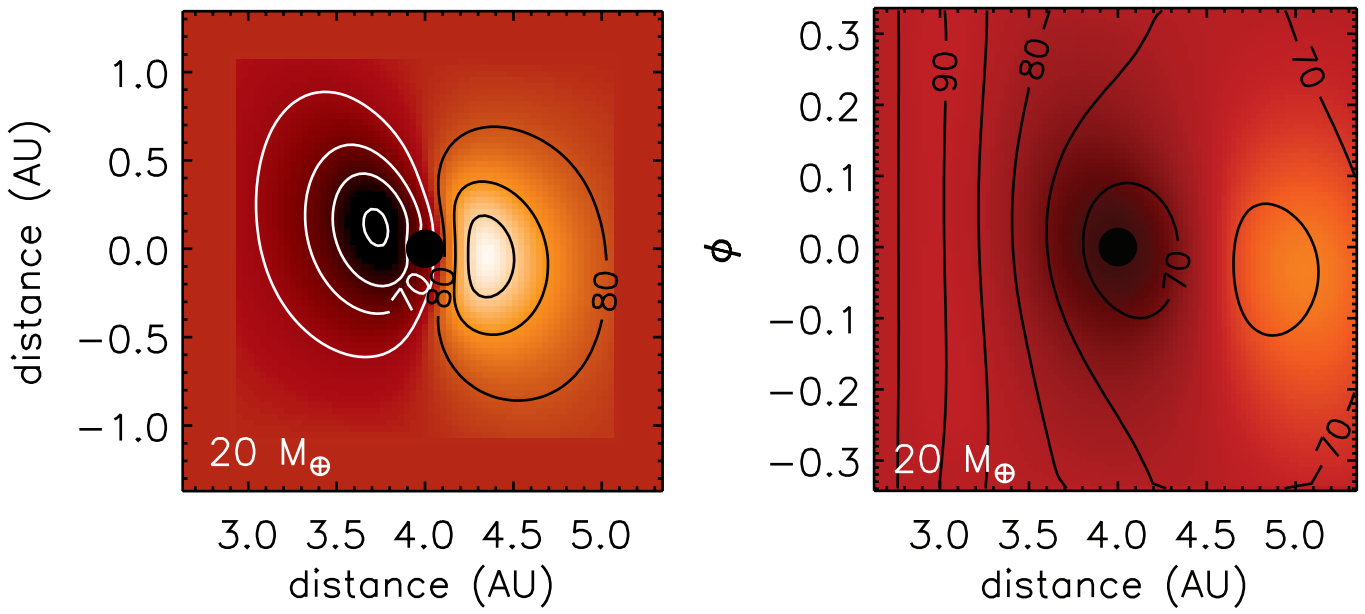

FIG. 12.— Temperature perturbations in the disk's photosphere above an embedded planet, as calculated in the J-CS model (*left*) and using the methods presented in this paper (*right*). Figures are scaled to the same spatial size, and colors represent fractional deviation from the unperturbed disk temperature. Contours show temperatures. Since the J-CS calculation assumed a plane-parallel disk, the temperature contours trace the color variations. In the calculation presented in this paper, the temperatures are dominated by the radial variation of the unperturbed disk.

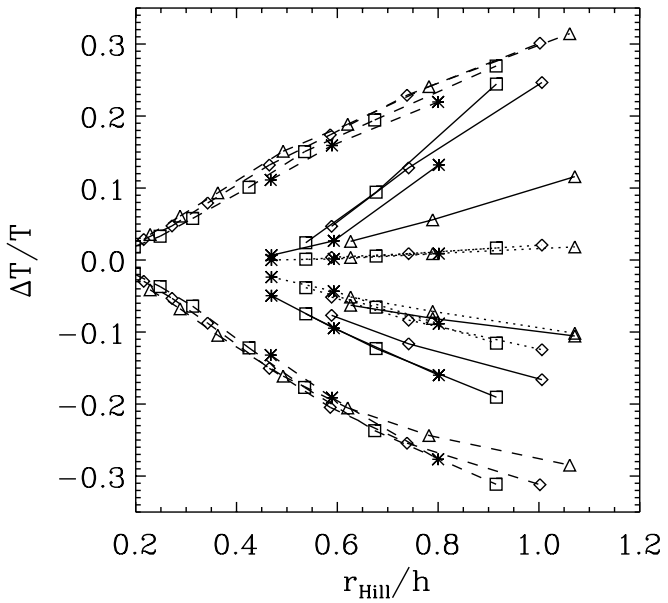

FIG. 13.—Maximum and minimum fractional temperature variation in the photosphere vs. $r_{\rm Hill}/h$. Symbols indicate planet distance as follows: triangles at 1 AU, diamonds at 2 AU, squares at 4 AU, and asterisks at 8 AU. Dashed lines show the J-CS model. Dotted lines show the current model, after only one iteration. Solid lines show the current model after 10 iterations. [*See the electronic edition of the Journal for a color version of this figure.*]

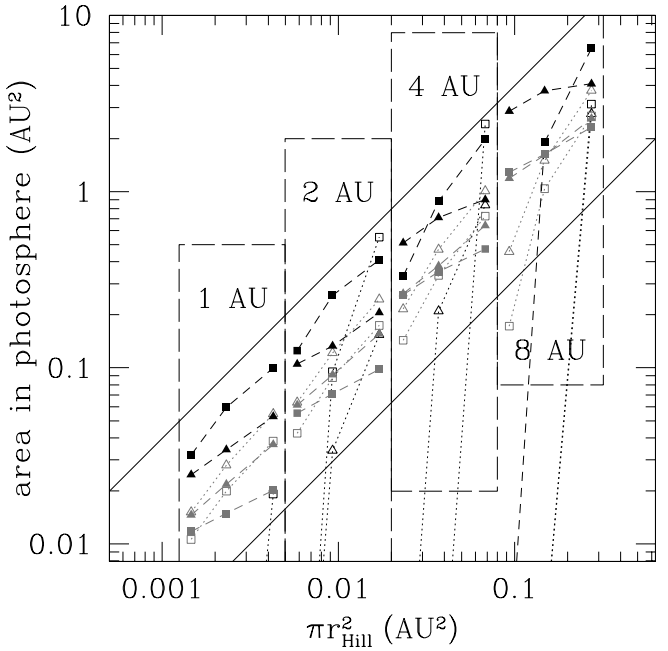

FIG. 14.—Areas of heated/cooled regions in the photosphere in current model (*black*) compared to results of previous model (*gray*). Horizontal axis is the area of a circle with radius of $r_{\rm hill}$. Planets with 10, 20, and 50 $M_\oplus$ at 1, 2, 4, and 8 AU are shown. The distances for each set of planets are indicated by the long-dashed boxes. Heated and cooled regions are represented by triangles and squares, respectively. Filled symbols connected by dashed lines show the areas heated/cooled beyond half the maximum temperature deviation in the photosphere. Open symbols connected by dotted lines show the areas that are heated/cooled beyond 10% above or below the unperturbed temperature. The diagonal solid lines show a linear slope. [*See the electronic edition of the Journal for a color version of this figure.*]

5.3. *Sizes of Thermally Perturbed Regions*

Although the variation in temperature appears to be less in the present model than that seen in J-CS, Figures 11 and 12 suggest that the spatial scale of the perturbations might be larger. To check this, we calculate the areas of the photosphere that are heated or cooled above or below a certain threshold. We call these regions hot or cold "spots." Note that this is different from the definition of a "spot" in Paper II, which considered regions heated above or below 170 K, in the context of ice formation and the snow line. Here we consider the deviation in temperature from the unperturbed value, rather than above or below a fixed threshold. A separate paper addressing the effect of these temperature perturbations on the snow line is presented by Jang-Condell et al. (2008).

We define the area of a spot to be the area of the photosphere that is heated or cooled to at least half the maximum temperature deviation, excluding the area just above the Hill sphere. These spot areas are plotted as filled triangles (hot) or squares (cold) in Figure 14 connected by dashed lines, black for the current models, gray for J-CS. The temperature deviations for the 10 $M_\oplus$ planet at 8 AU are so small that the area of a cold spot is not well defined. The spot masses are generally larger for our results than for the JC-S models. The sizes of cold spots tend to grow faster with increasing planet mass than the sizes of hot spots.

Let us also consider temperature perturbations above or below a threshold of 10%. The area of these spots versus the area of a circle with radius $r_{\rm Hill}$ is plotted as open triangles (hot) or squares (cold) in Figure 14 connected by dotted lines, black for the current models, gray for J-CS. Lines connected to points below the edge of the graph indicate lack of a spot. Note that at 1 AU, there are no hot spots above a 10% temperature deviation, consistent with Figure 13. The J-CS models produce hot and cold spots for planet parameters. At all distances, 10 $M_\oplus$ planets are too small to create either hot or cold spots at the 10% level in the new models. Where cold spots do exist, they are generally larger than those produced in J-CS. However, the hot spots are generally smaller.

While the temperature deviations predicted from the current models are not as great as those predicted in J-CS, they are larger in spatial extent. This may have consequences for the observability of this phenomenon. This topic will be addressed in a companion paper.

6. CONCLUSION

This paper presents a model for calculating the density and temperature perturbations imposed on a protoplanetary disk by an embedded protoplanet. The basic radiative transfer model is adopted from Papers I and II, but a number of improvements have been made on that work such as density-temperature self-consistency and eliminating the assumption of a plane-parallel system.

We have shown that self-consistently calculating the temperature and density significantly increases the effect of planet perturbations by means of postive feedback, where shadowed regions cool and contract and brightened regions heat and expand. This demonstrates the importance of self-consistency when calculating disk structure with radiative transfer. While it has already been acknowledged that stellar irradiation heating is important in setting overall disk structure (e.g., Chiang & Goldreich 1997; D'Alessio et al. 1998, 1999b; Dullemond & Dominik 2004), this work shows that it is important for considering local perturbations on the disk.

Another important result of this paper is that the temperature structure of the disk is extremely sensitive to the angle of incidence of stellar irradiation at the surface. The precise determination of the surface of the disk is critical to accurately calculating the temperature structure of the disk. In previous work we had assumed that the surface of constant density was a sufficiently

good approximatation for the surface, but in this work we show that that overestimated the temperature perturbation to the disk.

We have omitted some important physics in this calculation. We do not include heating from accretion onto the planet. We consider the embedded planet to act simply as a gravitational point mass, and focus only on the vertical component of gravity. We do not account for nonlinearities such as spiral density waves. All these effects are more adequately addressed using a three-dimensional hydrodynamic simulation of a planet embedded in a disk of gas. However, since simulations of this sort focus on the bulk flow of gas at the midplane, they typically have insufficient resolution above the midplane to accurately calculate the surface of the disk (e.g., Bate et al. 2003; Papaloizou et al. 2004; Klahr & Kley 2006; Oishi et al. 2007). Calculation of radiative transfer, even without iterating for self-consistency, is very computationally intensive. To do this iteratively and coupled with three-dimensional hydrodynamics is challenging but is the next logical step to improving the accuracy of our results.

This work was supported by the NASA Astrobiology Institute under cooperative agreement NNA04CC09A. Thanks also go to an anonymous referee for helpful suggestions for improving this paper.

REFERENCES

Bate, M. R., Lubow, S. H., Ogilvie, G. I., & Miller, K. A. 2003, MNRAS, 341, 213
Calvet, N., Patino, A., Magris, G. C., & D'Alessio, P. 1991, ApJ, 380, 617
Chiang, E. I., & Goldreich, P. 1997, ApJ, 490, 368
D'Alessio, P., Calvet, N., & Hartmann, L. 2001, ApJ, 553, 321
D'Alessio, P., Calvet, N., Hartmann, L., Lizano, S., & Cantó, J. 1999a, ApJ, 527, 893
D'Alessio, P., Cantó, J., Calvet, N., & Lizano, S. 1998, ApJ, 500, 411
D'Alessio, P., Cantó, J., Hartmann, L., Calvet, N., & Lizano, S. 1999b, ApJ, 511, 896
Dullemond, C. P., & Dominik, C. 2004, A&A, 417, 159
Hubickyj, O., Bodenheimer, P., & Lissauer, J. J. 2005, Icarus, 179, 415
Jang-Condell, H., Podolak, M., & Sasselov, D. 2008, ApJ, submitted
Jang-Condell, H., & Sasselov, D. D. 2003, ApJ, 593, 1116 (Paper I)
———. 2004, ApJ, 608, 497 (Paper II)
———. 2005, ApJ, 619, 1123
Klahr, H., & Kley, W. 2006, A&A, 445, 747
Oishi, J. S., Mac Low, M.-M., & Menou, K. 2007, ApJ, 670, 805
Paardekooper, S.-J., & Mellema, G. 2006, A&A, 459, L17
———. 2008, A&A, 478, 245
Papaloizou, J. C. B., Nelson, R. P., & Snellgrove, M. D. 2004, MNRAS, 350, 829
Pringle, J. E. 1981, ARA&A, 19, 137
Shakura, N. I., & Sunyaev, R. A. 1973, A&A, 24, 337
Siess, L., Dufour, E., & Forestini, M. 2000, A&A, 358, 593